Anisotropic magnetic properties of RCd$_{1-\delta}$Sb$_2$ (R = Ce–Nd) single crystals

Vikash Sharma ◎* and Arumugam Thamizhavel ◎†

Department of Condensed Matter Physics and Materials Science, Tata Institute of Fundamental Research,
Homi Bhabha Road, Colaba, Mumbai-400005, India

We report the magnetic properties of tetragonal compounds RCd$_{1-\delta}$Sb$_2$ (R = Ce–Nd) by means of magnetic susceptibility, heat capacity, and electrical resistivity measurements. A ferromagnetic ordering at $T_C \approx 3$ K, a nonmagnetic singlet ground state, and an antiferromagnetic ordering at $T_N \approx 2.4$ K is observed in CeCd$_{1-\delta}$Sb$_2$, PrCd$_{1-\delta}$Sb$_2$, and NdCd$_{1-\delta}$Sb$_2$, respectively. The trivalent nature of the rare-earth atoms has been confirmed from the effective magnetic moment estimated from the paramagnetic susceptibility data. The isothermal magnetization shows that the easy axis of magnetization is along the [100] direction for both CeCd$_{1-\delta}$Sb$_2$ and NdCd$_{1-\delta}$Sb$_2$. From the crystal electric field (CEF) analysis, based on the point charge model, we have analyzed the magnetic susceptibility, magnetization, and the heat capacity data and estimated the CEF split energy levels of CeCd$_{1-\delta}$Sb$_2$ and NdCd$_{1-\delta}$Sb$_2$.

I. INTRODUCTION

Rare-earth intermetallic compounds with the formula RTX_2, where R is rare earth element, T is transition metal, and X is pnictogen, show interesting magnetic properties and have been investigated quite extensively [1–9]. For instance, heavy fermion and Kondo behavior [1,3–5,7,10,11], nematic order [6], superconductivity [12], etc. have been observed in these types of compounds. It is interesting to note that these compounds crystallize in two different types of crystal structures, viz. ZrCuSi$_2$-type tetragonal structure with the space group $P4/nmm$ and HfCuSi$_2$-type orthorhombic structure with the space group $Pmca$ [7,10]. In particular, magnetic properties of RTSb$_2$ (T = Au, Ag, Cu, Pd, and Ni) family of compounds crystallizing in the ZrCuSi$_2$ type have been explored by several authors [1,3–6,8]. However, the reports on the magnetic properties of RCd$_{1-\delta}$Sb$_2$ are sparse [10] with only a detailed study on CeCd$_{1-\delta}$Sb$_2$, while the other rare earth compounds of the series have not been studied so far.

Generally, most of the Ce-based rare-earth compounds order antiferromagnetically, while the ferromagnetic ordering in Ce-based compounds are relatively less. The previous study on CeCd$_{1-\delta}$Sb$_2$ has revealed that it orders ferromagnetically at $T_C = 3$ K [10]. From a detailed study, Rosa *et al.* [10] reported that, depending on the c/a ratio of the lattice parameter, the nature of the ground state differs. For example, when the c/a ratio value ranges from 2.1 to 2.37, for CeTX$_2$ crystallizing in the ZrCuSi$_2$-type tetragonal structure an antiferromagnetic (AFM) order occurs, while for c/a more than 2.37 a ferromagnetic (FM) ground state is favored. Also the sign of the crystal field parameter (B_0^2) changes from negative to positive when the magnetic ordering changes from AFM to FM.

In view of these interesting physical properties exhibited by this series of compounds, we have synthesized RCd$_{1-\delta}$Sb$_2$ (R = Ce–Nd) single crystals using the flux method and characterized them using x-ray diffraction (XRD), energy dispersive analysis of x-ray (EDAX) and Laue diffraction. Their physical properties have been studied using temperature-dependent magnetic susceptibility $\chi(T)$, electrical transport $\rho(T)$, and heat capacity $C_p(T)$ measurements. The $\chi(T)$, $C_p(T)$, and $\rho(T)$ data reveal the FM ordering in CeCd$_{1-\delta}$Sb$_2$ at $T_C \approx 3$ K and AFM ordering in NdCd$_{1-\delta}$Sb$_2$ at $T_N \approx 2.4$ K, while PrCd$_{1-\delta}$Sb$_2$ shows paramagnetic behavior down to 1.8 K. We have observed significant anisotropy in $\chi(T)$ and isothermal magnetization $M(H)$ of RCd$_{1-\delta}$Sb$_2$ (R = Ce–Nd) along the two principal crystallographic directions, viz. [100] and [001]. In order to explain the anisotropic magnetic properties, we have analyzed the $\chi(T)$, $M(H)$, and $C_p(T)$ data in the framework of the CEF analysis based on the point charge model. The CEF analysis revealed a pure $|\pm 1/2\rangle$ ground state of CeCd$_{1-\delta}$Sb$_2$, which is in line with the earlier report [10]. The PrCd$_{1-\delta}$Sb$_2$ shows a singlet ground state that explains its paramagnetic behavior. The NdCd$_{1-\delta}$Sb$_2$ shows a doublet ground state, with AFM ordering.

II. EXPERIMENT

Single crystals of RCd$_{1-\delta}$Sb$_2$ (R = La–Nd) were grown by the high temperature solution growth method using excess composition of the stoichiometric CdSb, which melts congruently at 455 °C, as flux. The high-purity starting elements of Ce, Cd, and Sb in the molar ratio of 1:10.5:11.5 were placed in a high quality recrystallized alumina crucible and sealed under a high vacuum of 10^{-6} Torr in a quartz tube. The ampoule was heated to 1050 °C at a rate of 50 °C/h and held at this temperature for 48 h, before cooling it down to 550 °C at a rate of 2 °C/h. The excess flux was removed using a centrifuge. Flakelike single crystals of CeCd$_{1-\delta}$Sb$_2$ were obtained at the bottom of the crucible. Similarly, we have
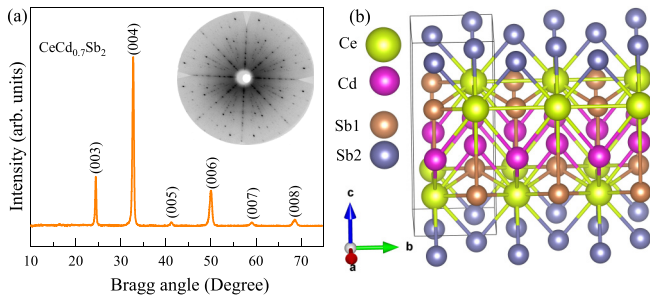
_____

*vikash.sharma@tifr.res.in
†thamiz@tifr.res.in

FIG. 1. (a) X-ray diffraction of a thin isolated single crystal of $CeCd_{1-\delta}Sb_2$, where the inset shows the Laue diffraction pattern of the (001) plane, and (b) crystal structure of $CeCdSb_2$.

obtained single crystals of $PrCd_{1-\delta}Sb_2$, $NdCd_{1-\delta}Sb_2$, and nonmagnetic $LaCd_{1-\delta}Sb_2$ by replacing the Ce with Pr, Nd, and La, respectively, with other reaction conditions remaining the same.

Powder x-ray diffraction (XRD) studies were performed using a PANalytical x-ray diffractometer equipped with a Cu-K_α monochromatic source, with wavelength $\lambda = 1.5406$ Å. The good quality of the grown crystals was ascertained from the Laue diffraction pattern. Also the crystals were aligned along the two principal crystallographic directions using the Laue diffraction. Field emission scanning electron microscope (FESEM) Zeiss ULTRA plus equipped with an energy dispersive x-ray (EDX) spectrometer was used to determine the composition of the grown single crystals. Magnetic measurements were performed using a superconducting quantum interference device–vibrating sample magnetometer (SQUID-VSM), Quantum Design, USA. Electrical and thermal transport measurements were performed in a physical property measurement system (PPMS), Quantum Design, USA. The electrical resistivity was measured by the four-point probe method along the [100] direction of the oriented single crystals. Gold wire with a diameter of 40 μm was used to make electrical contacts, using the silver paste, on the crystal surface.

III. RESULTS

A. Structural study

We performed XRD on a thin isolated single crystal of $CeCd_{1-\delta}Sb_2$ and the diffraction pattern is shown in Fig. 1(a). The XRD peaks are well indexed to (00*l*) family of planes, i.e., this crystal grows in the *ab* plane, which is typically the case for a *c*-axis long tetragonal system. Similar XRD patterns were obtained for $PrCd_{1-\delta}Sb_2$ and $NdCd_{1-\delta}Sb_2$, which are not shown here for brevity. The XRD of these compounds shows that they crystallize in the tetragonal crystal structure with the space group *P4/nmm* (no. 129). The crystal structure of stoichiometric $CeCdSb_2$ is shown in Fig. 1(b). The Ce and Cd atoms have only one site with 2*c* and 2*b* Wyckoff's position, respectively, while Sb atoms occupy two different Wyckoff's positions 2*a* and 2*c*. This structure has a stacking arrangement of *R*Sb-Cd-*R*Sb-Sb layers. We have estimated the lattice parameters from the XRD as $a = 4.330$ Å and $c = 10.932$ Å for $CeCd_{1-\delta}Sb_2$, $a = 4.323$ Å and $c = 10.871$ Å for $PrCd_{1-\delta}Sb_2$, and $a = 4.317$ Å and $c = 10.838$ Å

for $NdCd_{1-\delta}Sb_2$. The nearest distance between the Ce-Ce atoms is 4.330 Å, Pr-Pr atoms is 4.323 Å, and Nd-Nd atoms is 4.317 Å. The lattice parameters decrease when the *R* atom progresses from Ce to Nd, which is expected due to the size contraction of rare earth atoms. It is reported the magnetic ground state of $CeTX_2$ compounds highly depends on the dimensionality, i.e., *c/a* ratio [10]. When the *c/a* ratio falls within the range of 2.1 to 2.37, the compounds exhibit an AFM order [10]. However, for *c/a* ratios exceeding 2.37, a FM ground state becomes preferred for $CeTX_2$ compounds [10]. Note that our study involves three compounds with different rare earth atoms, viz. Ce, Pr, and Nd. The *c/a* ratio is approximately 2.5 for these compounds. Although the *c/a* ratio is nearly the same for these compounds $RCd_{0.7}Sb_2$ ($R =$ Ce–Nd), they have different magnetic ground state which may be attributed to different exchange interactions.

A representative Laue diffraction pattern of $CeCd_{1-\delta}Sb_2$ corresponding to the [001] direction is shown in the inset of Fig. 1(a). The well-defined spots of the Laue diffraction pattern confirm the good quality of the crystal. We have performed EDX measurements at different sites of single crystals to get the elemental composition. We have found nearly equal atomic percentages at different sites with variations less than about 2%. The EDX confirms the 1:0.7:2 ratio of the atomic percentage of *R*, Cd, and Sb, respectively. The deficiency at the transition metal site is usual in this family of compounds [10,13].

B. Magnetic properties of (La, Ce)Cd$_{0.7}$Sb$_2$

We first discuss the results of the nonmagnetic analog $LaCd_{0.7}Sb_2$. Figure 2(a) shows the $\chi(T)$ measured in an applied field of 2 kOe, for $H \parallel [100]$ of $LaCd_{0.7}Sb_2$ single crystal. As expected for a nonmagnetic system, the $\chi(T)$ of $LaCd_{0.7}Sb_2$ exhibits diamagnetic behavior in the entire temperature range, which is evident from Fig. 2. The upturn at low temperature is mainly attributed to the small amount of magnetic impurities present in the starting element(s). The temperature dependence of heat capacity of $LaCd_{0.7}Sb_2$ is shown in Fig. 2(b). Similar to the $\chi(T)$ data the heat capacity also did not show any magnetic transition down to 2 K. In order to estimate the Sommerfeld coefficient (γ) and the phononic contribution (β) to the heat capacity, we have plotted the low temperature heat capacity data in the form of C_p/T versus T^2 and fitted the data to the expression $C_p/T = \gamma + \beta T^2$ [Fig. 2(b) inset]. The estimated γ and β values are 0.532 mJ/(K^{2}mol) and 0.7975 mJ/(K^{4}mol), respectively. The low value of γ is typical for any metallic system without any strong correlations.

Temperature-dependent magnetization of $CeCd_{0.7}Sb_2$ measured in an applied magnetic field of 5 kOe along the two principle directions [100] and [001] is depicted in Fig. 3(a). There is a sharp increase in *M* at $T_C \approx 3$ K for both directions, which resembles the FM ordering in this compound. Figure 3(b) shows the inverse magnetic susceptibility of $CeCd_{0.7}Sb_2$. It is evident from the figure that there is a large anisotropy in the magnetic susceptibility. We have analyzed the $\chi^{-1}(T)$ data based on the modified Curie-Weiss (CW) law: $\chi(T) = \chi_0 + \mu_{\text{eff}}^2 n/[8(T - \theta_P)]$, where χ_0 is the temperature-independent contribution that
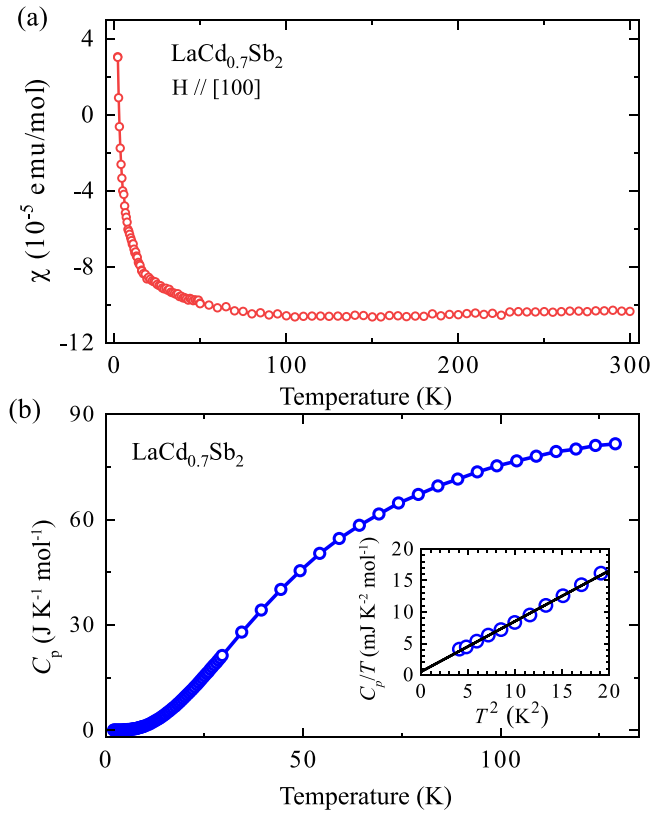
FIG. 2. (a) Magnetic susceptibility for $H \parallel [100]$ and (b) heat capacity of $LaCd_{0.7}Sb_2$, where the inset shows the low temperature region of the heat capacity, plotted as C_P/T versus T^2; the solid line is a fit to the experimental data.
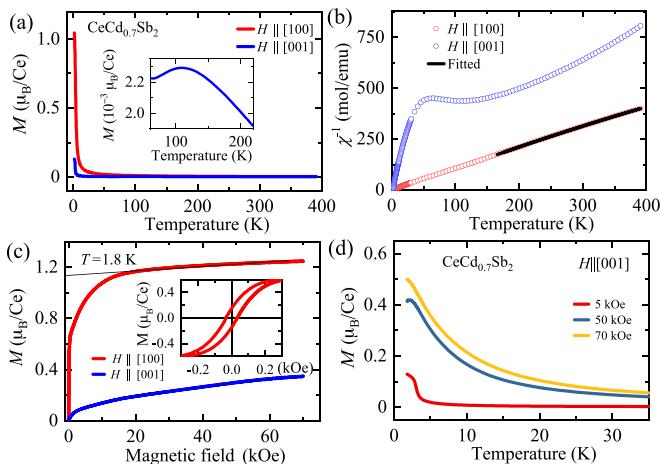

FIG. 3. (a) Temperature-dependent magnetization of $CeCd_{0.7}Sb_2$ for $H \parallel [100]$ and $H \parallel [001]$, where the inset shows the expanded view of $M(T)$ for $H \parallel [001]$, (b) inverse susceptibility fitted using the modified Curie-Weiss law for $H \parallel [100]$, (c) isothermal magnetization at 1.8 K along the two principal crystallographic directions, where the inset shows the expanded view near the origin for $H \parallel [100]$, and (d) $M(T)$ at different applied magnetic fields for $H \parallel [001]$, in the temperature range 2–35 K.

arises from the conduction electrons, n is the number of rare-earth atoms, here $n = 1$, and θ_p is the paramagnetic Weiss temperature and μ_{eff} is the effective magnetic moment [14]. The fit to the modified Curie-Weiss law is shown in Fig. 3(b) for $H \parallel [100]$. The μ_{eff} and θ_p for $H \parallel [100]$ is estimated to be 2.53 μ_B/Ce and 17 K, respectively, suggesting the trivalent nature of the Ce ion in this compound. The χ_0 is estimated to be 3.521×10^{-4} emu/mol. The deviation of CW behavior at low temperature is attributed to the crystal electric field (CEF) effect. However, for $H \parallel [001]$ direction the susceptibility data did not obey the modified CW law in this temperature range. This may be attributed to the broad humplike feature observed in M vs T data shown in the inset of Fig. 3(a). A similar inverse susceptibility behavior is observed by Rosa *et al.* [10].

Figure 3(c) shows the isothermal magnetization $M(H)$ of $CeCd_{0.7}Sb_2$ for $H \parallel [100]$ and $H \parallel [001]$, in the magnetically ordered state at 1.8 K. For $H \parallel [100]$, the M curve almost saturates at the low field of about 20 kOe with the saturation magnetization (M_s) of about 1.2 μ_B/Ce with a small hysteresis [Fig. 3(c) inset]. This shows the soft-FM behavior of this compound. This value of M_s is significantly smaller compared to the theoretical value of 2.14 for Ce^{3+}. The suppression of M_s in Ce-based compounds is generally attributed to the Kondo effect and CEF [10]. From the $M(H)$ at 1.8 K, we have estimated the spontaneous magnetization by extrapolating the high field data to zero field [Fig. 3(c)]. The spontaneous magnetization is found to be about 1.1 μ_B/Ce. However, it is important to perform neutron diffraction experiment to obtain the exact value of spontaneous magnetization.

For $H \parallel [001]$, $M(H)$ increases gradually with increasing field without any sign of saturation up to 70 kOe. These results clearly indicate that the [100] direction is the easy axis of magnetization, which is in good agreement with the higher value of $M(T)$ for $H \parallel [100]$ compared to $H \parallel [001]$. From the temperature-dependent magnetization [Fig. 3(a)], the ratio of M along [100] and [001] at T_C is found to be 42. Similarly, the ratio of isothermal magnetizations along [100] and [001] is found to be 3.6 at 1.8 K and 70 kOe [Fig. 3(c)]. Therefore, significant anisotropy in magnetic properties has been observed, which is explained using CEF splitting of the ground state multiplet of the degenerate $(2J + 1)$ levels of the Ce^{3+} ion, which will be discussed later.

Temperature-dependent magnetization at different applied magnetic fields for $H \parallel [001]$ is shown in Fig. 3(d). It can be seen that T_C is nearly suppressed at 50 kOe and completely wiped out at 70 kOe. Although $H \parallel [001]$ is the hard axis of magnetization, FM transition wipes out. This is in line with its soft FM behavior, as is evident from isothermal magnetization [Fig. 3(c)].

Figure 4(a) shows the temperature dependent C_p of $CeCd_{0.7}Sb_2$ and its nonmagnetic analog $LaCd_{0.7}Sb_2$. The C_p of $CeCd_{0.7}Sb_2$ shows a sharp jump at $T_C \approx 3$ K, which is in agreement with the FM transition as observed in the M vs T curve [Fig. 3(a)]. At high temperature, C_p saturates and attains the value of about 92 J $mol^{-1}K^{-1}$, which is close to the value of $3nR$ ($n = 3.7$, $R = 8.314$ J $mol^{-1}K^{-1}$; $3nR = 92.3$ J $mol^{-1}K^{-1}$), showing the validity of the Dulong–Petit law. The magnetic specific heat C_{mag} is calculated by subtracting the C_p

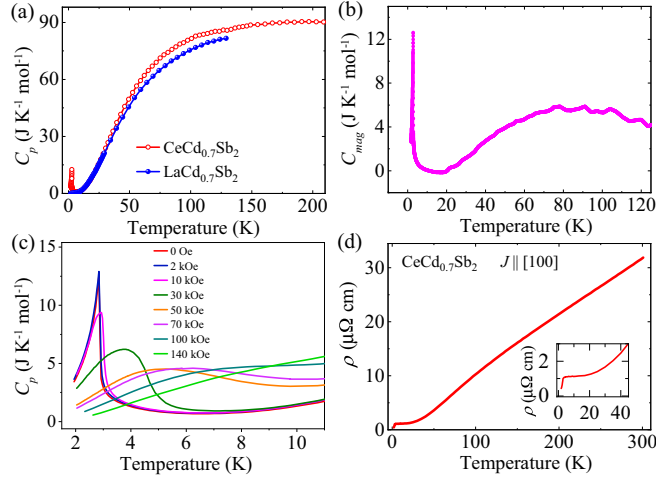FIG. 4. (a) Specific heat of CeCd$_{0.7}$Sb$_2$ along with nonmagnetic LaCd$_{0.7}$Sb$_2$, where the inset shows fitting of specific heat at low temperatures for LaCd$_{0.7}$Sb$_2$, (b) magnetic specific heat (C_{mag}), (c) specific heat at different applied magnetic fields along [001], and (d) electrical resistivity of CeCd$_{0.7}$Sb$_2$ for $J \parallel$ [100], where the inset shows the expanded view at low temperatures.

of LaCd$_{0.7}$Sb$_2$ from C_p of CeCd$_{0.7}$Sb$_2$ [Fig. 4(b)]. The C_{mag} shows a broad hump between 20 and 120 K, which is associated with the Schottky excitations arising from the splitting of Hund's ground-state multiplet. The jump in the magnetic part of the heat capacity ΔC_{mag} is found to be about 12.58 J/K mol. According to the mean field model, the jump in the C_{mag} at the ordering temperature for a spin half ($S = 1/2$) system is given by

$$\Delta C_{mag}(T_N) = 2.5R \left[\frac{(2S+1)^2 - 1}{(2S+1)^2 + 1} \right], \qquad (1)$$

where R is the gas constant. For $S = 1/2$, this amounts to 12.5 J/K mol. The ΔC_{mag} at $T_C = 3$ K [Fig. 4(b)] is close to the mean field value, which suggests the absence of the Kondo effect in CeCd$_{0.7}$Sb$_2$. Typically, this ΔC_{mag} value will be highly suppressed for a Kondo lattice compound [15,16].

We did not make an attempt to estimate the entropy as our C_p data was measured down to 2 K. Since this lowest data is very close to the magnetic ordering temperature of 3 K, the estimation of S_{mag} at T_C will lead to an erroneous value. However, the S_{mag} at T_C was obtained as 80% of $R \ln2$ by Rosa *et al.* [10], suggesting a doublet ground state of CeCd$_{0.7}$Sb$_2$.

The C_p at different applied magnetic fields along the hard axis of magnetization, $H \parallel$ [001], is shown in Fig. 4(c). The C_p peak broadens and moves toward higher temperature with an increase in the applied magnetic field. Such a higher temperature shift in C_p is a usual trend in the FM compound.

The electrical resistivity of CeCd$_{0.7}$Sb$_2$ for $J \parallel$ [100] is shown in Fig. 4(d). The ρ decreases with decrease in the temperature down to 15 K, it becomes nearly independent of temperature between 15 and 4 K, and finally suddenly drops at $T_C \approx 3$ K [Fig. 4(d) inset]. The sudden drop in ρ is due to the reduction in spin disorder scattering in the ordered state. The residual resistivity ratio (RRR), defined as $\rho_{300 \text{ K}}/\rho_{1.8 \text{ K}}$, is estimated as 74. This indicates the good quality of crystal in spite of the Cd deficiency present in the sample. A broad hump appearing in $\rho(T)$ at around 100 K suggests the thermal population of the crystal field split energy levels. It is to be mentioned here that the $\rho(T)$ of CeCd$_{0.7}$Sb$_2$ did not show any upturn at low temperatures, as it has been observed in the isostructural Kondo lattice compound CeAgSb$_2$ [17], suggesting the absence of Kondo effect in this compound. This is in accordance with the heat capacity data discussed above.

C. Magnetic properties of PrCd$_{0.7}$Sb$_2$

Figure 5(a) shows the temperature dependent $\chi(T)$ of PrCd$_{0.7}$Sb$_2$ for $H \parallel$ [100] and [001] measured in an applied field of 5 kOe. The $\chi(T)$ increases with the decrease in temperature down to 1.8 K without any signature of magnetic order, showing paramagnetic behavior in the temperature range 1.8 to 300 K. Further, to evaluate the higher temperature data, we have fitted inverse susceptibility for $H \parallel$ [100] and [001] using a modified CW law [Fig. 5(a) inset]. The value of μ_{eff} is found to 3.56 μ_B/Pr for both directions, which is close to the theoretical value of 3.58 μ_B/Pr for a trivalent Pr^{3+} ion. The θ_P for $H \parallel$ [100] and $H \parallel$ [001] are found to be 16.8
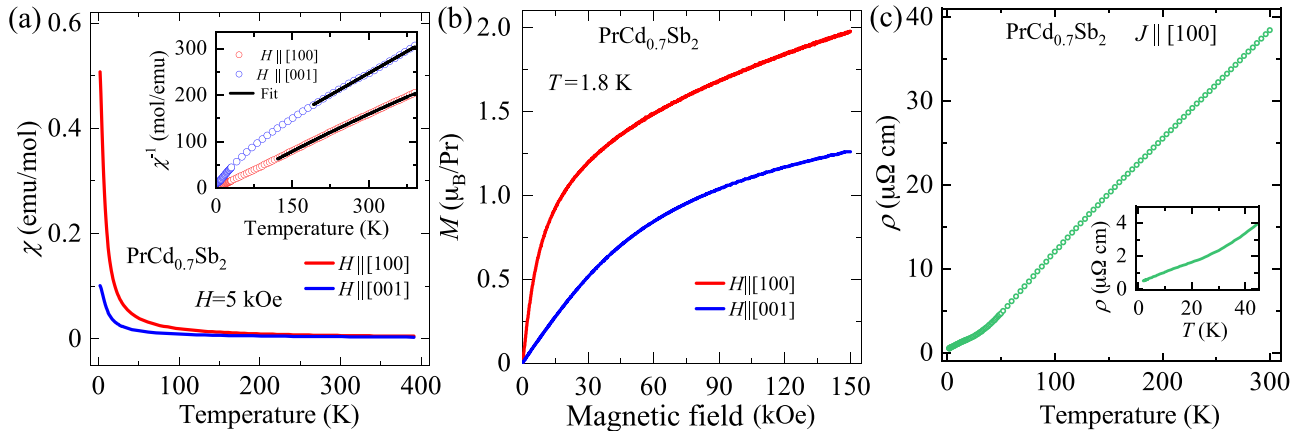

FIG. 5. (a) Temperature dependence of magnetic susceptibility of PrCd$_{0.7}$Sb$_2$ for $H \parallel$ [100] and $H \parallel$ [001], where the inset shows the inverse susceptibility fitted using the modified Curie-Weiss law, (b) isothermal magnetization measured at 1.8 K, and (c) temperature dependence of electrical resistivity for $J \parallel$ [100], where the inset shows the low temperature part.
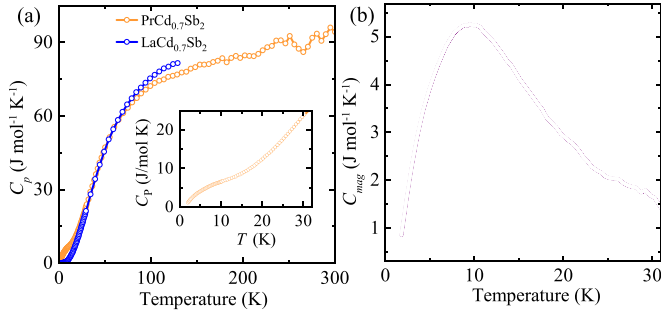
FIG. 6. (a) Specific heat of $PrCd_{0.7}Sb_2$ along with nonmagnetic $LaCd_{0.7}Sb_2$, where the inset shows the low temperature part, and (b) magnetic specific heat (C_{mag}) of $PrCd_{0.7}Sb_2$.

and -95.8 K, respectively, and χ_0 is about 6.284×10^{-4} and 1.693×10^{-5} emu/mol for $H \parallel [100]$ and $[001]$, respectively.

The isothermal $M(H)$ measured at 1.8 K increases monotonically with H, for fields up to 150 kOe along both the crystallographic directions [Fig. 5(b)], without any hysteresis, thus confirming the paramagnetic behavior. The $M(H)$ and $\chi(T)$ for $H \parallel [100]$ attain the higher value compared to $H \parallel [001]$. They show significant anisotropy along these two principal crystallographic directions. The absence of magnetic ordering in $PrCd_{0.7}Sb_2$ is attributed to a singlet ground state.

Figure 5(c) shows $\rho(T)$ in the temperature range 2 to 300 K of $PrCd_{0.7}Sb_2$ for $J \parallel [100]$. It is evident that $\rho(T)$ decreases with decrease in the temperature without any signature of magnetic ordering down to 2 K, revealing a typical metallic

behavior. The RRR is estimated as 77, which indicates the good quality of the crystal.

The $C_p(T)$ of $PrCd_{0.7}Sb_2$ along with nonmagnetic $LaCd_{0.7}Sb_2$ is shown in Fig. 6(a). The C_p of $PrCd_{0.7}Sb_2$ increases as temperature increases with a broad shoulder centered around 10 K [Fig. 6(a) inset]. This can be correlated with low-lying CEF states that are getting populated by thermal energy. The C_p attains a value of about $3nR$ at room temperature. The $LaCd_{0.7}Sb_2$ has a relatively smaller value of C_p below 40 K. However, C_p of $LaCd_{0.7}Sb_2$ dominates over the $PrCd_{0.7}Sb_2$ above 50 K. This difference in specific heat at high temperatures could be due to different phonon contributions to the C_p for both compounds. The C_{mag} shows a broad peak at 10 K, which may be due to low lying CEF states which are being populated due to thermal energy [Fig. 6(b)].

D. Magnetic properties of $NdCd_{0.7}Sb_2$

Figure 7(a) shows $\chi(T)$ of $NdCd_{0.7}Sb_2$ for $H \parallel [100]$ and $[001]$ measured in an applied magnetic field of 5 kOe. The $\chi(T)$ for both directions increases with decrease in the temperature and suddenly drops at $T_N \approx 2.4$ K due to the AFM ordering of the Nd moments. We have analyzed the inverse susceptibility for $H \parallel [100]$ and $[001]$ using modified CW law [Fig. 7(a) inset]. The CW law gives reasonable fitting at high temperatures. The μ_{eff} is found to be about $3.60 \, \mu_B$/Nd for both directions, which is close to the theoretical value of $3.62 \, \mu_B$/Nd. The θ_P is found to be 5.7 K and -44.3 K for $H \parallel [100]$ and $[001]$, respectively, and χ_0 is about -6.406×10^{-4} and 7.054×10^{-4} emu/mol for $H \parallel [001]$ and $[001]$, respectively. Usually, θ_P takes negative value for AFM
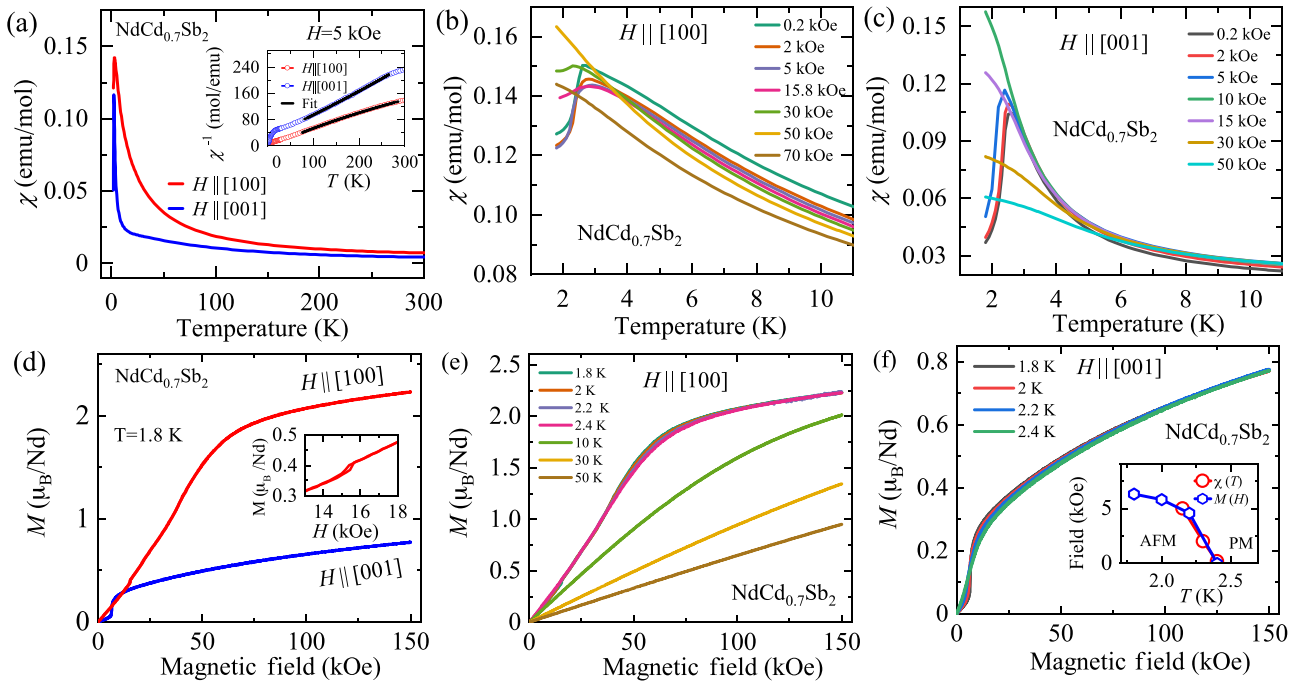
FIG. 7. (a) Temperature dependent magnetic susceptibility of $NdCd_{0.7}Sb_2$, where the inset shows inverse susceptibility fitted using the modified Curie-Weiss law for $H \parallel [100]$ and $H \parallel [001]$. (b), (c) Magnetic susceptibility at different fields, (d) isothermal magnetization, and (e), (f) isothermal magnetization at different temperatures for $H \parallel [100]$ and $H \parallel [001]$, respectively, of $NdCd_{0.7}Sb_2$; inset (f) shows the magnetic phase diagram for $H \parallel [001]$ direction derived from the magnetic susceptibility and from the temperature dependence of the metamagnetic transition.

compounds and positive value for FM compounds. However, the opposite sign of θ_P has previously been observed in this series of compounds due to significant anisotropy in the paramagnetic regime appearing due to CEF [10,18].

The $\chi(T)$ for $H \parallel$ [100] and [001] measured at different applied magnetic fields is shown in Figs. 7(b) and 7(c), respectively. For $H \parallel$ [100], the T_N associated with AFM ordering broadens and shifts more or less towards lower temperatures with the increase in an applied magnetic field up to 30 kOe and it wipes out at 50 kOe [Fig. 7(b)]. Similarly, T_N broadens and shifts towards lower temperatures up to 5 kOe and it gets completely suppressed at 10 kOe for $H \parallel$ [001] [Fig. 7(c)]. Such suppression in AFM ordering at low fields appears to indicate a soft AFM behavior of $NdCd_{0.7}Sb_2$.

Further, we have measured the isothermal magnetization at 1.8 K for $H \parallel$ [100] and [001] [Fig. 7(d)]. For $H \parallel$ [100], $M(H)$ increases rapidly in a linear fashion up to 60 kOe, where it changes slope and shows a sluggish increase with field. It attains a value of 2.2 μ_B/Nd at 150 kOe, which is smaller than the theoretical value of saturation magnetization $g_J J$ $(8/11 \times 9/2 = 3.27) \mu_s = 3.27 \mu_B$/Nd. It seems that it probably will attain the saturation value at higher magnetic fields. The change in slope and a tiny hysteresis around 15.8 kOe can be seen in the magnetization plot [Fig. 7(d) inset]. This feature appears to indicate spin reorientation transition about 15.8 kOe. For $H \parallel$ [001], $M(H)$ increases linearly up to 6.3 kOe, where it shows a sudden jump in magnetization and then, from 7 kOe, it monotonically increases. This metamagnetic transition suggests a field-induced change in the magnetic structure of $NdCd_{0.7}Sb_2$. The larger value of isothermal $M(H)$ and $\chi(T)$ for $H \parallel$ [100] indicates that it is an easy axis of magnetization, while $H \parallel$ [001] is the hard axis. However, the T_N gets suppressed at a lower field of 10 kOe for the hard axis [001] compared to that of 50 kOe for an easy axis [100] [Figs. 7(b) and 7(c)]. This may be attributed to the metamagnetic transition that appeared along the hard axis, viz. [001] direction.

Magnetic isotherms for $H \parallel$ [100] and $H \parallel$ [001] at different temperatures are shown in Figs. 7(e) and 7(f), respectively. For $H \parallel$ [100], as temperature increases, the $M(H)$ shows the same trend below $T_N \approx 2.4$ K and a tiny hysteresis observed at 15.8 kOe disappears at 2.4 K. Above $T_N \approx 2.4$ K, M curves increase monotonically and the magnetic moment decreases with increase in the temperature, showing paramagnetic behavior as expected above T_N. Similarly, in the case of $H \parallel$ [001], the $M(H)$ shows the same trend from 1.8 K to 2.2 K with gradual suppression of the metamagnetic transition [Fig. 7(f) inset]. This feature completely disappears at $T_N \approx 2.4$ K, which is expected at and above the ordered state. We have constructed a magnetic phase diagram for $H \parallel$ [100] from the field dependence of magnetic susceptibility and the temperature dependence of isothermal magnetization by tracing the metamagnetic transition. The tentative magnetic phase diagram is shown in the inset of Fig. 7(f), which demarcates the paramagnetic (PM) and AFM regions.

Figure 8 shows C_p of $NdCd_{0.7}Sb_2$ for $H \parallel$ [001] along with its nonmagnetic analog $LaCd_{0.7}Sb_2$. The C_p of $NdCd_{0.7}Sb_2$ shows a sharp anomaly at $T_N = 2.4$ K, which is associated with the AFM transition. The C_{mag} shows a broad hump at around 25 K, which is attributed to the Schottky excitations
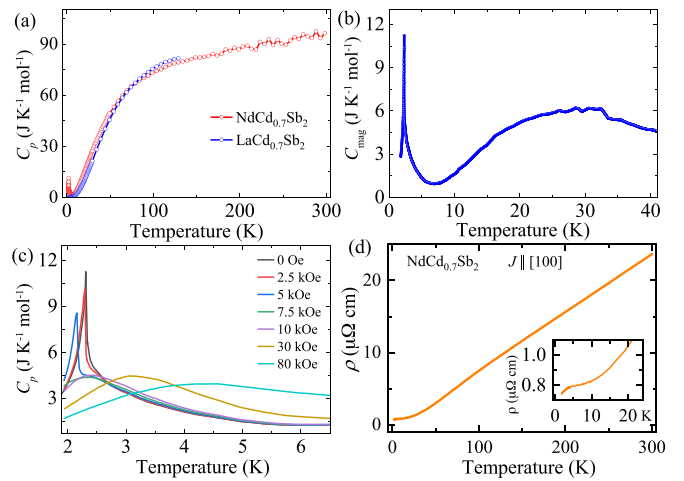

FIG. 8. (a) Specific heat of $NdCd_{0.7}Sb_2$ along with nonmagnetic $LaCd_{0.7}Sb_2$, (b) magnetic specific heat (C_{mag}), (c) specific heat of $NdCd_{0.7}Sb_2$ at different applied magnetic fields along [001], and (d) electrical resistivity of $NdCd_{0.7}Sb_2$ for $J \parallel$ [100].

arising from the splitting of the CEF-split Hund's ground-state multiplet. The details about the CEF-split energy levels are discussed later. The C_p changes quite interestingly with the application of magnetic field [Fig. 8(c)]. As the field increases up to 5 kOe, the peak of C_p shifts towards the lower temperatures, which is a usual trend for the AFM systems. However, a further increase in the magnetic field leads the C_p peak to shift towards the higher temperature side, which is quite unusual for an AFM system. The heat capacity peak gets broadened and shifted towards lower (higher) temperatures for an AFM (FM) system with the increase in field. Here, for fields greater than 5 kOe, the heat capacity peak gets broadened and shifts towards higher temperature side signals the field induced FM interactions in $NdCd_{0.7}Sb_2$, as also observed in the $M(H)$ for $H \parallel$ [001].

Electrical resistivity of $NdCd_{0.7}Sb_2$ for $J \parallel$ [100] is shown in Fig. 8(d). The $\rho(T)$ decreases with decrease in the temperature down to 7 K and becomes nearly independent of the temperature between 4 and 7 K, showing metallic behavior. It gradually decreases below 4 K since magnetic scattering becomes coherent near and below T_N [Fig. 8(d) inset]. The RRR is found to be about 32 for $NdCd_{0.7}Sb_2$, which is quite high and suggests the good quality of the grown crystal.

E. Discussion

From the magnetic studies it is evident that there is a considerable anisotropy in the $RCd_{0.7}Sb_2$ system exhibiting different magnetic ground states. The anisotropy in the magnetization studies can be explained by the CEF analysis. In order to determine the CEF level schemes of $RCd_{0.7}Sb_2$ compounds, we analyzed the $(\chi - \chi_0)^{-1}$ data based on the point charge model [19]. In these compounds, the R atom occupies the $2c$ Wyckoff position, which has a point symmetry that corresponds to the tetragonal site symmetry. The tetragonal CEF Hamiltonian is given by

$$\mathcal{H}_{CEF} = B_2^0 O_2^0 + B_4^0 O_4^0 + B_4^4 O_4^4 + B_6^0 O_6^0 + B_6^4 O_6^4, \quad (2)$$

where B_l^m and O_l^m are the crystal field parameters and Steven's operators, respectively [19,20].

We used the Hamiltonian described in Eq. (2) for $NdCd_{0.7}Sb_2$ to obtain the energy eigenvalues and the eigenfunctions. In the case of $CeCd_{0.7}Sb_2$, the sixth order terms vanish, i.e., last two terms of Eq. (2) will be zero. Since $PrCd_{0.7}Sb_2$ does not order magnetically down to 2 K, it is evident that the ground state must be a singlet ground state. We employed the CEF analysis only for $CeCd_{0.7}Sb_2$ and $NdCd_{0.7}Sb_2$ magnetically ordered systems.

Furthermore, the CEF Hamiltonian can be used to estimate the CEF susceptibility. The CEF susceptibility is given by the expression

$$\chi_{CEFi} = N(g_J\mu_B)^2 \frac{1}{Z}\left(\sum_{m\neq n} |\langle m|J_i|n\rangle|^2 \frac{1-e^{-\beta\Delta_{m,n}}}{\Delta_{m,n}} e^{-\beta E_n} \right.$$

$$\left. + \sum_n |\langle n|J_i|n\rangle|^2 \beta e^{-\beta E_n} \right), \qquad (3)$$

where g_J is the Landé g factor; E_n and $|n\rangle$ are the nth eigenvalue and eigenfunction, respectively. The $\mathbf{J}_i$ ($i = x$, y, and z) is a component of the angular momentum, and $\Delta_{m,n} = E_m - E_n$, $Z = \sum_n e^{-\beta E_n}$, and $\beta = 1/k_B T$. The Z and N are the partition function and the Avogadro number, respectively.

The magnetic susceptibility including the molecular field contribution λ_i ($i = x, y, z$) is given by

$$\chi_i^{-1} = \chi_{CEFi}^{-1} - \lambda_i. \qquad (4)$$

We have analyzed the isothermal magnetization based on the CEF model with the following Hamiltonian:

$$\mathcal{H} = \mathcal{H}_{CEF} - g_J\mu_B J_i(H + \lambda_i M_i), \qquad (5)$$

where $\mathcal{H}_{CEF}$ is the CEF Hamiltonian defined in Eq. (5), and the second and third terms are the Zeeman term and the molecular field term, respectively. The magnetization M_i is defined as

$$M_i = g_J\mu_B \sum_n |\langle n|J_i|n\rangle| \frac{\exp(-\beta E_n)}{Z} \quad (i = x, y, z). \qquad (6)$$

The inverse magnetic susceptibility calculated based on Eq. (3) is shown in Fig. 9. The CEF analysis explains the observed anisotropy, reasonably well, in the paramagnetic state of both $CeCd_{0.7}Sb_2$ and $NdCd_{0.7}Sb_2$. Since the inverse susceptibility data for $CeCd_{0.7}Sb_2$ along $H \parallel [001]$ did not yield a proper μ_{eff} value, we have fitted the paramagnetic susceptibility by fixing the μ_{eff} value to 2.54 μ_B/Ce and estimated the χ_0 value. We subtracted the obtained χ_0 values (-7.3251×10^{-5} and 1.37619×10^{-4} emu/mol for $H \parallel [100]$ and [001] directions, respectively, for $CeCd_{0.7}Sb_2$ and 1.241×10^{-3} and 1.433×10^{-3} emu/mol for $H \parallel [100]$ and [001] directions, respectively, for $NdCd_{0.7}Sb_2$) with the susceptibility data and used the resultant data for the CEF analysis. A similar approach has been made by Takeuchi *et al.* for $CePt_3Si$ [21]. The CEF parameters thus obtained are listed in Tables I and II for these two compounds. The calculated CEF susceptibility matches well in the high temperature paramagnetic region; however, at low temperature there is a deviation from the experimental data. It is necessary to consider the Zeeman and the anisotropic exchange terms in the CEF Hamiltonian
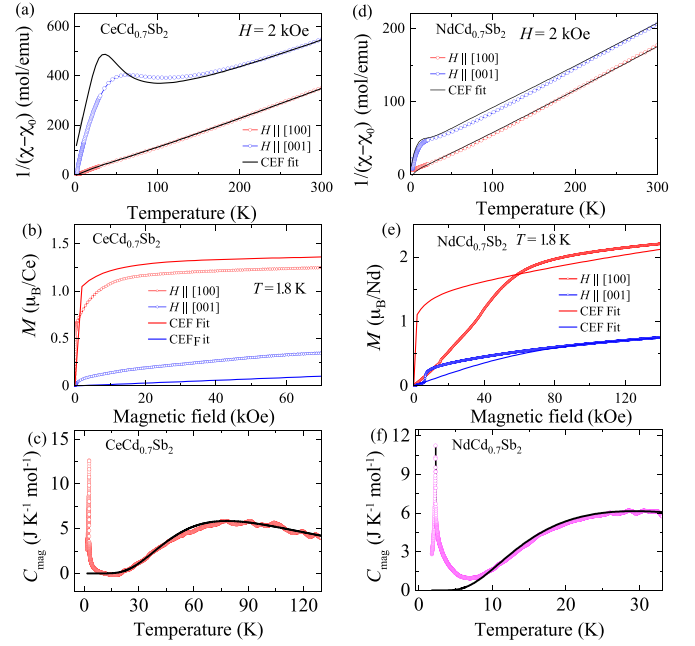

FIG. 9. CEF fit of (a), (d) inverse magnetic susceptibility, (b), (e) isothermal magnetization, and (c), (f) Schottky heat capacity of $CeCd_{0.7}Sb_2$ and $NdCd_{0.7}Sb_2$, respectively.

[22] to obtain a better fit of the low temperature data, which is beyond the scope of the present manuscript. The energy eigenvalues and eigenfunctions are obtained by diagonalizing the CEF Hamiltonian. For the Ce ion, $S = 1/2$, $L = 3$ and hence $J = 5/2$ possesses sixfold degenerate levels; similarly for the Nd ion, $S = 3/2$, $L = 6$ and hence $J = 9/2$ possesses tenfold degenerate levels. Both Ce and Nd atoms have odd number of electrons and hence are Kramer's ions. For the Ce atom, with half integer J value, $J = 5/2$ in the noncubic symmetry will have a total of three levels, while for the Nd atom, with $J = 9/2$ will have five levels. As indicated in Table I, for the Ce atom the sixfold degenerate levels split into three doubles with an overall splitting energy of 269 K. Similarly for the Nd atom, the tenfold degenerate levels split

TABLE I. CEF parameters, energy level, and wave functions of the CEF scheme obtained from the thermodynamic properties of $CeCd_{0.7}Sb_2$.

CEF parameters			
B_2^0 (K)	B_4^0 (K)	B_4^4 (K)	λ_i (emu/mol)$^{-1}$
6.7	−0.71	1.55	$\lambda_x = 4$, $\lambda_z = -93$
Energy levels and wave functions			

E (K)	$|5/2\rangle$	$|3/2\rangle$	$|1/2\rangle$	$|-1/2\rangle$	$|-3/2\rangle$	$|-5/2\rangle$
269	0	0.931	0	0	0	0.364
269	0.364	0	0	0	0.931	0
147	0.931	0	0	0	−0.364	0
147	0	−0.364	0	0	0	0.931
0	0	0	0	1	0	0
0	0	0	1	0	0	0

TABLE II. CEF parameters, energy level, and wave functions of the CEF scheme obtained from the thermodynamic properties of NdCd$_{0.7}$Sb$_2$.

CEF parameters									
B_2^0 (K)	B_4^0 (K)	B_4^4 (K)	B_6^0 (K)	B_6^4 (K)	λ_i (emu/mol)$^{-1}$				
1.237	0.0014	−0.1823	0.0018	0.0172	$\lambda_x = 4, \lambda_z = -4$				
Energy levels					Wave functions				
E (K)	$\lvert 9/2\rangle$	$\lvert 7/2\rangle$	$\lvert 5/2\rangle$	$\lvert 3/2\rangle$	$\lvert 1/2\rangle$	$\lvert -1/2\rangle$	$\lvert -3/2\rangle$	$\lvert -5/2\rangle$	$\lvert -7/2\rangle$	$\lvert -9/2\rangle$
329	0	0	0	−0.637	0	0	0	0.771	0	0
329	0	0	0.771	0	0	0	−0.637	0	0	0
257	0	−0.035	0	0	0	0.396	0	0	0	0.917
257	0.917	0	0	0	0.396	0	0	0	−0.035	0
73	0	0	0	0.771	0	0	0	0.637	0	0
73	0	0	0.637	0	0	0	0.771	0	0	0
61	0.141	0	0	0	−0.242	0	0	0	0.96	0
61	0	0.96	0	0	0	−0.242	0	0	0	0.141
0	0	0.278	0	0	0	0.886	0	0	0	−0.372
0	−0.372	0	0	0	0.886	0	0	0	0.278	0

into five doublets with an overall splitting energy of 329 K. The ground state of CeCd$_{0.7}$Sb$_2$ is a purely $\lvert \pm 1/2\rangle$ state, while the first and second excited states are dominated by $\lvert \pm 3/2\rangle$ and $\lvert \pm 5/2\rangle$ states, respectively. For NdCd$_{0.7}$Sb$_2$ the ground state is a doublet ground state.

It is evident from Figs. 9(b) and 9(e) that the obtained set of crystal field parameters qualitatively explain the easy and hard axes of magnetization in both CeCd$_{0.7}$Sb$_2$ and NdCd$_{0.7}$Sb$_2$. The molecular field constant λ represents the exchange interactions between the rare-earth ions and is highly anisotropic. The λ is positive for $H \parallel [100]$ and negative for [001] direction, which is consistent with the paramagnetic Weiss temperature discussed earlier. We further used the CEF energy levels to obtain the Schottky heat capacity as shown in Figs. 9(c) and 9(f). The Schottky heat capacity has been estimated using the Eq. (6) given in Ref. [23]. It is clear

that these energy levels reproduce the Schottky heat capacity which is associated with the broad humplike feature in C_{mag}. Our estimated values of the CEF energy levels for CeCd$_{0.7}$Sb$_2$ match with the published results of Rosa *et al.* [10]. However, inelastic neutron diffraction measurements are necessary to confirm the estimated energy levels from the magnetization and heat capacity data.

Next, we turn our discussions to the ground state of CeCd$_{0.7}$Sb$_2$, which is a purely $\lvert \pm 1/2\rangle$ state. For a purely $\lvert \pm 1/2\rangle$ state, one would expect a magnetization value of $g_J J_z \mu_B = (6/7 \times 1/2 = 0.43\,\mu_B/\mathrm{Ce})$. However, in the present case we observe saturation values of $1.1\,\mu_B/\mathrm{Ce}$ for $H \parallel [100]$ and $0.35\,\mu_B/\mathrm{Ce}$ for $H \parallel [001]$. The larger magnetization for $H \parallel [100]$ is a characteristic feature of the $\lvert \pm 1/2\rangle$ ground state due to the large in-plane $J_{x,y}$ component, which can be induced with the application of a perpendicular magnetic field. A similar behavior has been observed in the isostructural CeAgSb$_2$, which also exhibits a purely $\lvert \pm 1/2\rangle$ ground state, with the magnetization along the [100] direction larger than the [001] direction [22]. In Fig. 10 we show the calculated magnetization plot at $T = 2$ K with the CEF parameters shown in Table I. The calculated CEF magnetization shows a large value for $H \parallel [100]$ compared to that of the [001] direction. Along the [001] direction a large plateaulike feature with a magnetization value of $0.43\,\mu_B/\mathrm{Ce}$ is observed, which is consistent with the $\lvert \pm 1/2\rangle$ state. At about 150 T there is a sudden rise in the magnetization for $H \parallel [100]$, which saturates to $2.1\,\mu_B/\mathrm{Ce}$ at about 260 T. The sharp increase in the magnetization at 150 T is attributed to the level crossing effect due to the high magnetic field. It will be interesting to study the magnetic structure of CeCd$_{0.7}$Sb$_2$ using neutron diffraction.
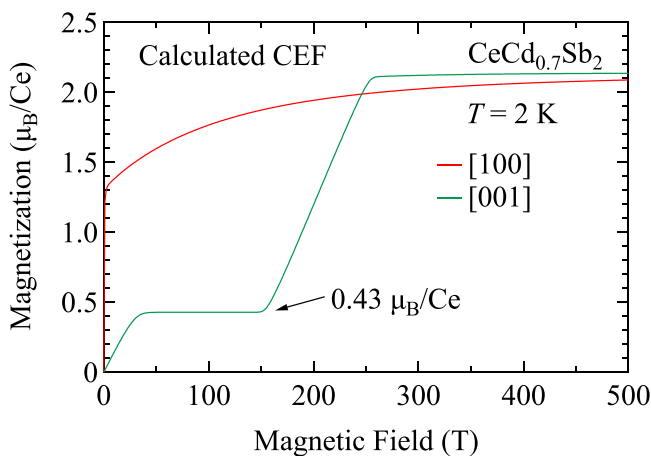

FIG. 10. Calculated CEF magnetization (CEF parameters are given in Table I) of CeCd$_{0.7}$Sb$_2$ at $T = 2$ K along the two principal crystallographic directions. The sudden rise in the magnetization at about 150 T for $H \parallel [001]$ direction is mainly attributed to the CEF level crossings at high magnetic fields.

IV. CONCLUSION

We have studied the anisotropic magnetic properties of RCd$_{1-\delta}$Sb$_2$ (R = Ce–Nd) single crystals. The CeCd$_{1-\delta}$Sb$_2$ shows a ferromagnetic ordering at $T_C \approx 3$ K and NdCd$_{1-\delta}$Sb$_2$

shows an antiferromagnetic ordering at $T_N \approx 2.4$ K. However, $PrCd_{1-\delta}Sb_2$ did not show any magnetic ordering down to 1.8 K, showing paramagnetic behavior. The $H \parallel [100]$ is found to be the easy axis of magnetization for $CeCd_{1-\delta}Sb_2$ and $NdCd_{1-\delta}Sb_2$ from the magnetic susceptibility and isothermal magnetization studies. Interestingly, the isothermal magnetization of $NdCd_{1-\delta}Sb_2$ exhibits a metamagnetic transition with a tiny hysteresis along the easy axis of magnetization, which is associated with spin reorientation. The electrical resistivity and magnetic heat capacity show the absence of Kondo effect in $CeCd_{0.7}Sb_2$. These compounds show significant magnetic anisotropy along two principle directions, viz. [100] and [001]. We have analyzed the magnetocrystalline anisotropy based on the point charge model. The obtained CEF scheme revealed a doublet ground state for $CeCd_{1-\delta}Sb_2$ and $NdCd_{1-\delta}Sb_2$.

[1] E. Jobiliong, J. S. Brooks, E. S. Choi, H. Lee, and Z. Fisk, Magnetization and electrical-transport investigation of the dense kondo system $CeAgSb_2$, Phys. Rev. B **72**, 104428 (2005).

[2] E. V. Sampathkumaran, K. Sengupta, S. Rayaprol, K. K. Iyer, T. Doert, and J. P. F. Jemetio, Enhanced electrical resistivity before Néel order in the metals $RCuAs_2$ (R = Sm, Gd, Tb, and Dy), Phys. Rev. Lett. **91**, 036603 (2003).

[3] S. Seo, V. A. Sidorov, H. Lee, D. Jang, Z. Fisk, J. D. Thompson, and T. Park, Pressure effects on the heavy-fermion antiferromagnet $CeAuSb_2$, Phys. Rev. B **85**, 205145 (2012).

[4] A. Thamizhavel, T. Takeuchi, T. Okubo, M. Yamada, R. Asai, S. Kirita, A. Galatanu, E. Yamamoto, T. Ebihara, Y. Inada, R. Settai, and Y. Ōnuki, Anisotropic electrical and magnetic properties of $CeTSb_2$ (T = Cu, Au, and Ni) single crystals, Phys. Rev. B **68**, 054427 (2003).

[5] Y. Muro, N. Takeda, and M. Ishikawa, Magnetic and transport properties of dense kondo systems, $CeTSb_2$ (T = Ni, Cu, Pd and Ag), J. Alloys Compd. **257**, 23 (1997).

[6] S. Seo, X. Wang, S. M. Thomas, M. C. Rahn, D. Carmo, F. Ronning, E. D. Bauer, R. D. dos Reis, M. Janoschek, J. D. Thompson, R. M. Fernandes, and P. F. S. Rosa, Nematic state in $CeAuSb_2$, Phys. Rev. X **10**, 011035 (2020).

[7] R. Mondal, R. Bapat, S. K. Dhar, and A. Thamizhavel, Magnetocrystalline anisotropy in the Kondo-lattice compound $CeAgAs_2$, Phys. Rev. B **98**, 115160 (2018).

[8] R. Y. Chen, J. L. Liu, L. Y. Shi, C. N. Wang, S. J. Zhang, and N. L. Wang, Possible orbital crossover in the ferromagnetic Kondo lattice compound $CeAgSb_2$, Phys. Rev. B **99**, 205107 (2019).

[9] T. Park, V. A. Sidorov, H. Lee, Z. Fisk, and J. D. Thompson, Pressure-tuned first-order phase transition and accompanying resistivity anomaly in $CeZn_{1-\delta}Sb_2$, Phys. Rev. B **72**, 060410(R) (2005).

[10] P. F. S. Rosa, R. J. Bourg, C. B. R. Jesus, P. G. Pagliuso, and Z. Fisk, Role of dimensionality in the Kondo $CetX_2$ family: The case of $CeCd_{0.7}Sb_2$, Phys. Rev. B **92**, 134421 (2015).

[11] D. Evans, S. Dunsiger, and E. Mun, Anisotropic magnetism and antiferromagnetic ordering in the Kondo-lattice compound $YbCuAs_2$, Phys. Rev. B **105**, 085105 (2022).

[12] K. Kodama, S. Wakimoto, N. Igawa, S. Shamoto, H. Mizoguchi, and H. Hosono, Crystal and magnetic structures of the superconductor $CeNi_{0.8}Bi_2$, Phys. Rev. B **83**, 214512 (2011).

[13] P. Wollesen, W. Jeitschko, M. Brylak, and L. Dietrich, Ternary antimonides $LnM_{1-x}Sb_2$ with Ln=La-Nd, Sm, Gd, Tb and M=Mn, Co, Au, Zn, Cd, J. Alloys Compd. **245**, L5 (1996).

[14] Y. Li, S. M. Winter, D. A. S. Kaib, K. Riedl, and R. Valentí, Modified Curie-Weiss law for j_{eff} magnets, Phys. Rev. B **103**, L220408 (2021).

[15] P. K. Das, N. Kumar, R. Kulkarni, and A. Thamizhavel, Magnetic properties of the heavy-fermion antiferromagnet $CeMg_3$, Phys. Rev. B **83**, 134416 (2011).

[16] E. D. Mun, S. L. Bud'ko, A. Kreyssig, and P. C. Canfield, Tuning low-temperature physical properties of $CeNiGe_3$ by magnetic field, Phys. Rev. B **82**, 054424 (2010).

[17] K. Myers, S. Bud'ko, I. Fisher, Z. Islam, H. Kleinke, A. Lacerda, and P. Canfield, Systematic study of anisotropic transport and magnetic properties of $RAgSb_2$ (R= Y, La-Nd, Sm, Gd-Tm), J. Magn. Magn. Mater. **205**, 27 (1999).

[18] X. Wu, W. He, T. Yang, G. Xiao, P. Chen, Y. Bi, and W. Wu, The magnetic and electronic properties of $REAgSb_2$ compounds, J. Magn. Magn. Mater. **519**, 167442 (2021).

[19] M. Hutchings, Point-charge calculations of energy levels of magnetic ions in crystalline electric fields, Solid State Phys. **16**, 227 (1964).

[20] K. Stevens, Matrix elements and operator equivalents connected with the magnetic properties of rare earth ions, Proc. Phys. Soc. A **65**, 209 (1952).

[21] T. Takeuchi, S. Hashimoto, T. Yasuda, H. Shishido, T. Ueda, M. Yamada, Y. Obiraki, M. Shiimoto, H. Kohara, T. Yamamoto *et al.*, Magnetism and superconductivity in a heavy-fermion superconductor, $CePt_3Si$, J. Phys.: Condens. Matter **16**, L333 (2004).

[22] S. Araki, N. Metoki, A. Galatanu, E. Yamamoto, A. Thamizhavel, and Y. Ōnuki, Crystal structure, magnetic ordering, and magnetic excitation in the $4f$-localized ferromagnet $CeAgSb_2$, Phys. Rev. B **68**, 024408 (2003).

[23] D. A. Joshi, A. K. Nigam, S. K. Dhar, and A. Thamizhavel, Thermal and transport behavior of single-crystalline R_2CoGa_8 (R = Gd, Tb, Dy, Ho, Er, Tm, Lu, and Y) compounds, Phys. Rev. B **80**, 054414 (2009).